Coastal Engineering 47 (2003) 381–398

Coastal Engineering
An International Journal for Coastal, Harbour and Offshore Engineers

www.elsevier.com/locate/coastaleng

A synchronously coupled tide–wave–surge model of the Yellow Sea

Byung Ho Choi[a,*], Hyun Min Eum[a], Seung Buhm Woo[b]

[a] *Department of Civil and Environmental Engineering, Sungkyunkwan University, Suwon 440-746, South Korea*
[b] *School of Civil and Environmental Engineering, Cornell University, Ithaca, NY 14853, USA*

Received 28 March 2002; received in revised form 20 September 2002; accepted 16 October 2002

Abstract

A coupled wave–tide–surge model has been established in this study in order to investigate the effect of tides, storm surges, and wind waves interactions during a winter monsoon on November 1983 in the Yellow Sea. The coupled model is based on the synchronous dynamic coupling of a third-generation wave model, WAM-Cycle 4, and the two-dimensional tide–surge model. The surface stress generated by interactions between wind and waves is calculated using the WAM-Cycle 4 directly based on an analytical approximation of the results obtained from the quasi-linear theory of wave generation. The changes of bottom friction factor generated by waves and current interactions are calculated by using simplified bottom boundary layer model. The model simulations showed that bottom velocity and effective bottom drag coefficient induced by combination of wave and current were increased in shallow waters of up to 50 m in the Yellow Sea during the wintertime strong storm conditions.

Keywords: Synchronously coupled model; Shallow water; Surge; Tide; Wave modelling; Winter monsoon

1. Introduction

The Yellow and East China Seas form a complex oceanographic system with considerable spatial and temporal variations in physical properties and behavior (Fig. 1). The region is most remarkable for its large tides along the west coast of Korea, mideast Chinese coast, and for complexity of tidal phenomena along with seasonally varying monsoon, typhoons, fresh water discharges from surrounding land masses, and the Kuroshio. During the severe storm conditions, the interactions among tide, wave, and storm surge processes are pronounced within the shallow sea basin.

During the recent years, significant efforts were made for developing high-resolution spectral wave model to deal with shallow water conditions and incorporating the interaction due to tide and surge under EU-MAST III PROMISE project (Monbaliu et al., 2000; Prandle, 2000; Ozer et al., 2000). Especially, Ozer et al. (2000) developed a generic module, in which WAM-Cycle 4 model and two-dimensional shallow water wave hydrodynamic model are coupled for combined modelling of tides, surges, and waves. They applied the coupled model to the North Sea and

* Corresponding author. Tel.: +82-31-290-7512; fax: +82-31-290-7549.
E-mail address: bhchoi@yurim.skku.ac.kr (B.H. Choi).

0378-3839/02/$ - see front matter
PII: S0378-3839(02)00143-6

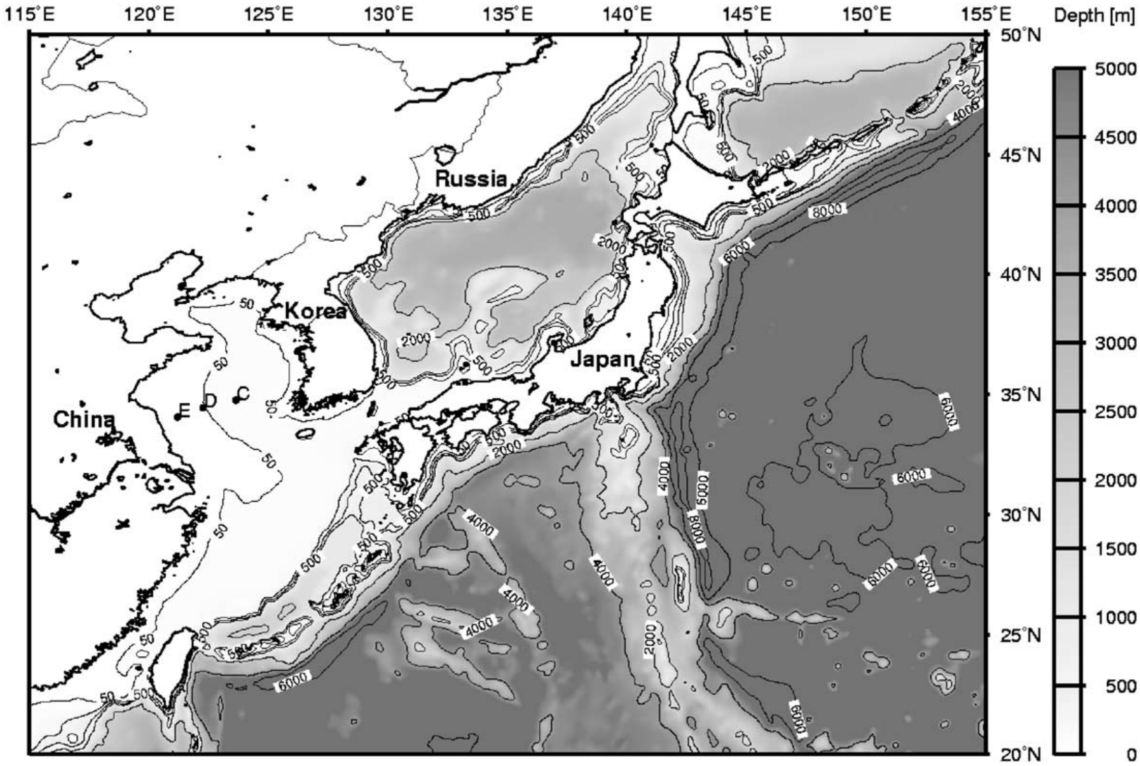

Fig. 1. Model area for the study with three current mooring positions (C, D, and E) during November 1983.

found that the sensitivity of waves to coupling effects increases from deep to shallow water. For the region of the South and East China Seas, previous modelling studies (Zhang and Li, 1996; Li and Zhang, 1997; Moon, 2000) have been performed to investigate the interaction of waves and currents by the dynamical coupling of a third-generation wave model and a storm surge model. They showed that the surface wave-dependent drag has significant effect on surges.

However, the wave-induced enhancement of bottom stress generated by the tidal- and surge-induced currents has not been fully explored by the previous works. In the present study, a synchronously coupled wave–tide–surge model is established, in which the theory of wave-dependent surface roughness (Janssen, 1991) is applied for upper surface condition, and the simplified bottom boundary layer model of Grant and Madsen (1986) is used for bottom boundary condition. An initial attempt has been made to investigate the influence of combined waves and currents on bottom dissipations incorporating into the dynamically coupled manners in the model.

The established model was then used to simulate a winter monsoon of November 1983, when the moored current observations were made by Woods Hole Oceanographic Institution (WHOI) in off-southern Shandong Peninsula. In the previous study, Graber et al. (1989) indicated that sediment transport dynamics in the Yellow and East China Seas are strongly coupled to the action of wind-generated surface waves during intense winter storms. Their study was focused to the wave-induced bottom flows inducing sediment resuspension with regards to present-day distribution of bottom sediments in the region based on finite-depth wind wave model (Graber and Madsen, 1985). The positions of the three points are shown in Fig. 1. In this paper, some of the preliminary results aiming to advance modelling of wave–tide–surge interactions under strong winter monsoon in the Yellow Sea are presented and discussed.

2. Numerical model

2.1. Wave model

The third-generation wave model, WAM-Cycle 4, is one of the most sophisticated and validated model in the world (WAMDI Group, 1988), and integrates the basic transport equation describing the evolution of a two-dimensional ocean wave spectrum without additional assumptions with respect to the spectral shape. The three source functions describing the wind input, nonlinear transfer, and whitecapping dissipation are prescribed explicitly. In addition to the source functions, bottom dissipation and refraction terms are incorporated to the model of the finite-depth version. The evolution of a two-dimensional ocean wave spectrum $F(f, \theta, \phi, \lambda, t)$ with respect to frequency, f, and direction, θ (measured clockwise relative to true north), as a function of latitude, ϕ, and longitude, λ, on the spherical earth is governed by the transport equation

$$\frac{\partial F}{\partial t} + (\cos\phi)^{-1}\frac{\partial}{\partial \phi}(\dot{\phi}\cos\phi F) + \frac{\partial}{\partial \lambda}(\dot{\lambda}F) + \frac{\partial}{\partial \theta}(\dot{\theta}F) = S, \tag{1}$$

where S is the net source function describing the change of energy of a propagating wave group and

$$\dot{\phi} = \frac{\mathrm{d}\phi}{\mathrm{d}t} = vR^{-1}\cos\theta, \tag{2}$$

$$\dot{\lambda} = \frac{\mathrm{d}\lambda}{\mathrm{d}t} = v\sin\theta(R\cos\phi)^{-1}, \tag{3}$$

$$\dot{\theta} = \frac{\mathrm{d}\theta}{\mathrm{d}t} = v\sin\theta\tan\phi R^{-1} \tag{4}$$

represent the rates of change of the position and propagation direction of a wave packet traveling along a great circle path. Here, $v = g/4\pi f$ denotes the group velocity, g the acceleration of gravity, and R the radius of the earth. The right-hand side of Eq. (1) represents the effects of wave generation and dissipation including wave generation by wind, nonlinear resonant wave interactions, whitecapping, and wave energy dissipation due to bottom friction. The linear theory of surface gravity waves with wave number (k) and frequency (ω) are interrelated in the dispersion relation as follows:

$$\omega = \sigma + \vec{k}\vec{U} \tag{5}$$

$$\sigma^2 = gk \tanh kd \tag{6}$$

where ω ($=2\pi f_{\mathrm{a}}$) is the absolute radian frequency observed in a frame of reference fixed to the bottom and σ ($=2\pi f_{\mathrm{r}}$) is the relative frequency observed in a frame of reference that moves with the mean current velocity $\vec{U}$, and f_{a} and f_{r} are the absolute and relative frequencies, respectively. $\vec{k}$ is the wave number vector with absolute value of k, and g is the acceleration of gravity.

The model was calibrated with respect to the fetch-limited wave growth data. Only two tuning parameters are introduced in the whitecapping dissipation source function. The model is well explained by Günther et al. (1992) and its scientific, basic, and actual implementation are also described by Komen et al. (1994). Considerable enhancements to the WAM-Cycle 4 model have been made under EU-MAST III PROMISE project for applications on shelf scale and interacting with tides on coastal scale (Monbaliu et al., 1999). In our study, some modifications on WAM-Cycle 4 model code were made to accommodate unsteady elevations and currents from the tide and surge model and to avoid garden-sprinkler effect (Tolman, 2002). Despite insufficient physical understanding of the processes governing the evolution and dissipation, model prediction is very satisfactory in terms of practical point of view because some empirical relations of the processes are skillfully incorporated into the model.

2.2. Tide and surge model

The vertically integrated equations in spherical coordinates for tides and storm surges incorporate a quadratic law of bottom friction with the nonlinear advective terms. The equations are given by:

$$\frac{\partial \xi}{\partial t} + \frac{1}{R\cos\phi}\left\{\frac{\partial(dU)}{\partial x} + \frac{\partial(dV\cos\phi)}{\partial \phi}\right\} = 0, \tag{7}$$

$$\frac{\partial U}{\partial t} - 2\omega\sin\phi V + \frac{U}{R\cos\phi}\frac{\partial U}{\partial x} + \frac{V}{R\cos\phi}\frac{\partial}{\partial\phi}(U\cos\phi) = \frac{-g}{R\cos\phi}\frac{\partial\xi}{\partial x} - \frac{1}{\rho R\cos\phi}\frac{\partial P}{\partial x}\frac{k_b U(U^2+V^2)^{1/2}}{d} + \frac{F^{(s)}}{\rho d} \tag{8}$$

$$\frac{\partial V}{\partial t} - 2\omega\sin\phi U + \frac{U}{R\cos\phi}\frac{\partial U}{\partial x} + \frac{V}{R}\frac{\partial V}{\partial\phi} = \frac{-g}{R}\frac{\partial\xi}{\partial\phi} - \frac{1}{\rho R}\frac{\partial P}{\partial\phi} - \frac{k_b V(U^2+V^2)^{1/2}}{d} + \frac{G^{(s)}}{\rho dL} \tag{9}$$

where the notation is as follows:

x, ϕ	east-longitude and north-latitude, respectively
t	time
ξ	elevation of sea surface
h	undisturbed depth of water
$d=h+\xi$	total depth of water
R	radius of the Earth
ω	angular speed of the Earth's rotation
g	acceleration due to gravity
$F^{(s)}$, $G^{(s)}$	components of wind stress on sea surface to the east and the north, respectively
P	atmospheric pressure at the sea surface
U, V	components of the depth–mean current are given by $U = \frac{1}{h+\xi}\int_{\xi}^{-h} u(z)\mathrm{d}z$, $V = \frac{1}{h+\xi}\int_{\xi}^{-h} v(z)\mathrm{d}z$
$u(z)$, $v(z)$	components of current in the direction of increasing x and ϕ, respectively, at a depth of z below the undisturbed sea surface
k_b	the coefficient of quadratic bottom friction and 0.0025 for this study

Eqs. (7)–(9) are discretized in time and space with the use of a simple one-step forward time difference and a staggered spatial grid, in which ξ, U, and V are calculated at different grid points. This grid scheme has been used previously in discretizing the hydrodynamics equation (Choi, 1980). The nonlinear advective terms are incorporated using the 'angled derivative' method suggested by Roberts and Weiss (1967). The method centers the advective term in time domain, effectively damping the high-frequency waves generated by the nonlinearities. Thus, the difference scheme is explicit and employs forward and backward differences for time and central difference for space. In order to solve Eqs. (7)–(9), it is necessary to specify both initial and boundary conditions. Along the coastline boundaries, the current component normal to the boundary is set to zero and a radiation condition for the open boundaries is used to prevent the artificial reflection of disturbances generated in the model. The open boundary condition is specified in terms of a function of position and time as follows,

$$q_n = q_n^{\mathrm{M}} + q_n^{\mathrm{T}} + \frac{c}{h}(\xi - \xi^{\mathrm{M}} - \xi^{\mathrm{T}}) \tag{10}$$

where $c=(gh)^{1/2}$, q_n^{M}, and ξ^{M} are the inputs of meteorological origin, and q_n^{T} and ξ^{T} are the inputs of tidal origin. The tidal inputs of q_n^{T} and ξ^{T} are expressed in standard harmonic form, as follows:

$$\xi^{\mathrm{T}} = \sum_{i=1}^{n} f_i H_i \cos(\eta_i t + u_i + V_i - G_i) \tag{11}$$

$$q_n^{\mathrm{T}} = \sum_{i=1}^{n} f_i Q_i \cos(\eta_i t + u_i + V_i - G_i) \tag{12}$$

where H_i, Q_i, and G_i, for normal component of depth–mean currents of the ith constituent, denote the harmonic constants, amplitudes, and phases of tidal elevation, respectively; η_i is the speed; n is the number of constituent; V_i is the phase of corresponding equilibrium constituent at Greenwich at time $t=0$ (the start of a hindcast); and f_i and u_i are nodal factors allowing for the 18.6 years variation in amplitude and phase of the constituents. The values of V_i, f_i, and u_i are computed at the start of each hindcast suggested by Doodson (1921). The constants for the tide model are given by the previous model experiment (Choi, 1980) and only M_2, S_2, K_1, and O_1 constituents are used. The surge input of q_n^{M} and ξ_n^{M} is assumed as

$$q_n^{\mathrm{M}} = 0, \xi^{\mathrm{M}} = (\bar{p}_a - p_a)/\rho g \tag{13}$$

where $\bar{p}_a$ is 1013 mb and p_a is the atmospheric pressure at the sea surface.

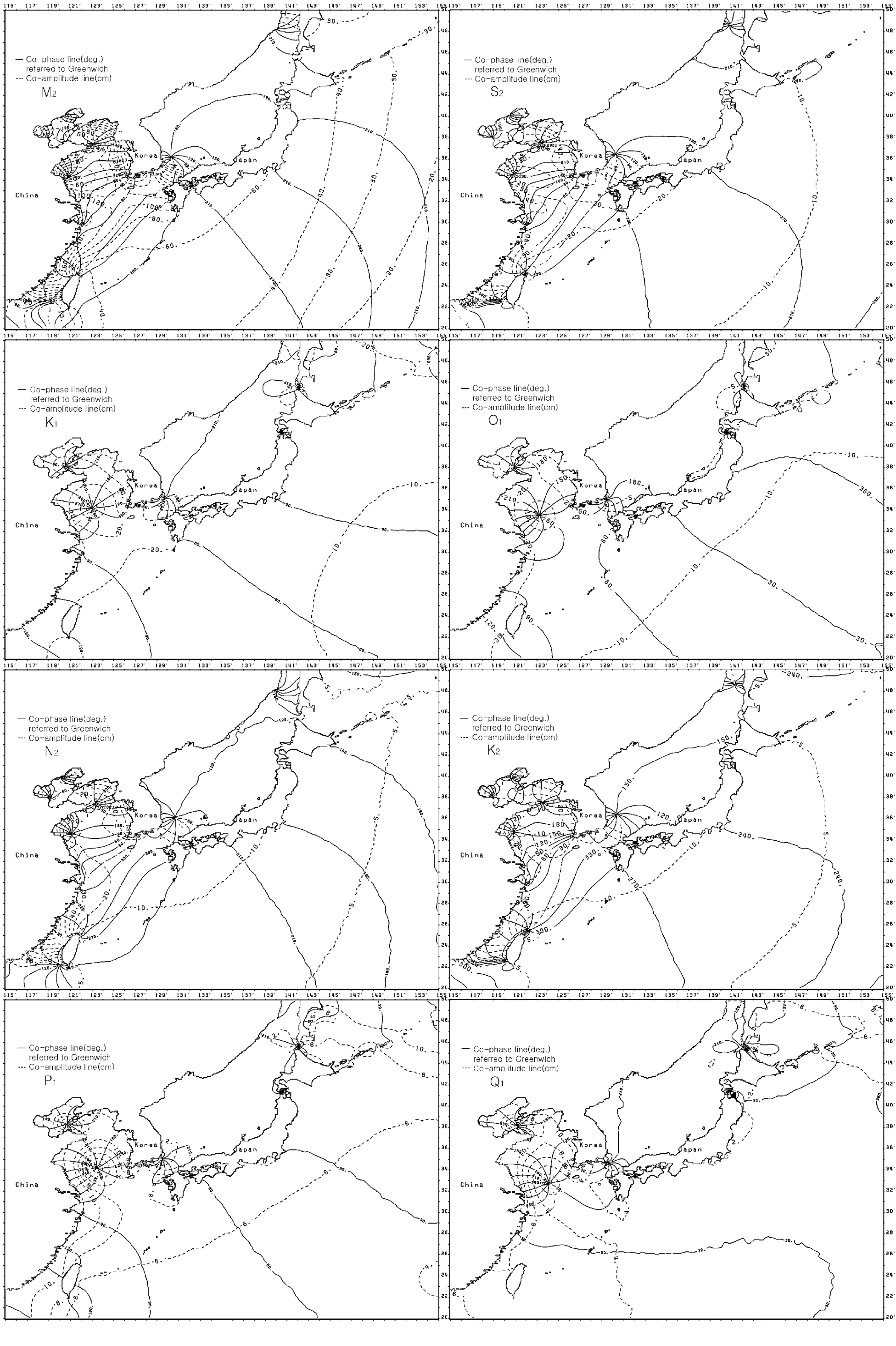

Fig. 2. Computed cotidal charts of the M_2, S_2, K_1, O_1, N_2, K_2, P_1, and Q_1 tides.

With the numerical models covering the Northwest Pacific region, the water movements associated with real-time tides and actual storms can be reproduced. Reasonably well representative model simulations with the coastal data observed can lead to estimate the extreme condition of waves and currents for the design of coastal defense and offshore structures. The model employed here was developed originally at the Institute of Oceanographic Sciences (IOS) (Choi, 1980) to explore general tidal dynamics of the Yellow Sea. This model was improved and extended to cover wider region from previous model (Choi, 1980) and to include additional major tidal components (Choi, 1987, 1993). The model is two-dimensional, implementing nonlinear depth-averaged hydrodynamical equations in spherical polar coordinate. The model has the east and north components of current on the grid system of 1/12° latitudes by 1/12° longitudes utilizing Digital Bathymetric Data Base 5 min (DBDB5) with a modification of water depths in the Yellow Sea area (Choi et al., 2002). The model has 481×361 grid elements with a selected time step of 40 s. Open boundary conditions of the tidal model for East Asian Marginal Seas have been selected for this model with the model resolution of 1/6° (Choi and Ko, 1994), from which the computed M_2, S_2, K_1, O_1, N_2,

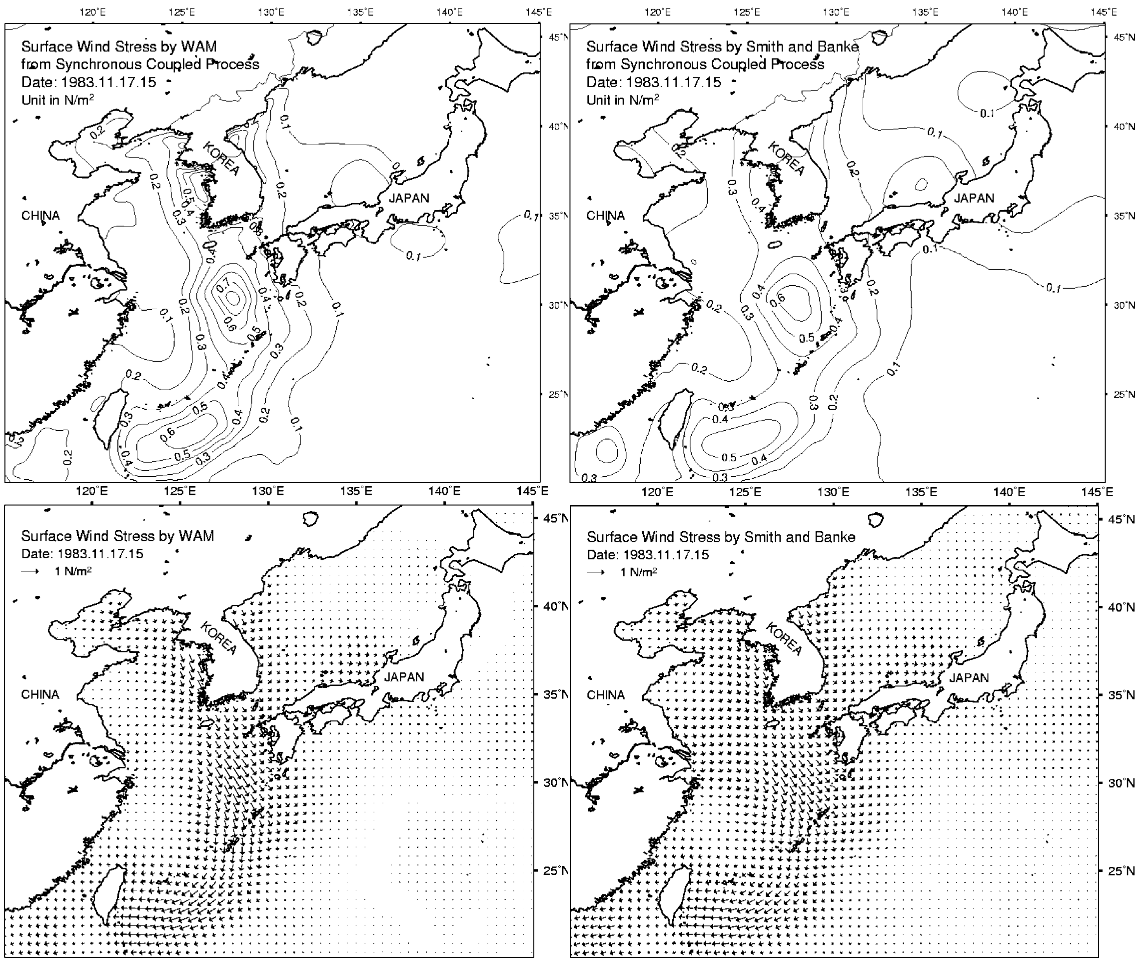

Fig. 3. Comparison between surface wind stress using the total stress including wave-dependent stress from WAM model (left) and conventional wind stress formulation (e.g. Smith and Banke, 1975; right) during winter monsoon in November 1983.

K_2, P_1, and Q_1 tidal charts are provided in Fig. 2. Along the open boundary, eight major tidal constituents can be prescribed for real-time tide specification.

2.3. Surface wind stress and simplified bottom boundary layer model

Janssen (1991) concluded that the growth rate of the waves generated by wind depends on a number of additional factors, such as the atmospheric density stratification, wind gustiness, and wave age and gave a more realistic parameterization of the interaction between wind and wave. Heaps (1983) had already identified the need for a wave model to improve the specification of wind stress in surge models. Mastenbroek et al. (1993) clearly show the influence of a wave-dependent surface drag coefficient on surge elevations. Even if these surge elevations can be reproduced with an appropriate tuning of this parameter in conventional wind stress formulations (e.g. the dimensionless constant in the Charnock relation) (Charnock, 1955), they argue that a wave-dependent drag is to be preferred for storm surge modelling. Davies and Lawrence (1994) notice a significant change of the tidal amplitude and phase in shallow near-coastal regions due to enhanced frictional effects associated with wind-driven flow and wind wave turbulence.

The total surface stress consists of a turbulent and wave-dependent term as follows

$$\tau = \tau_t + \tau_w \tag{14}$$

where τ_t is the turbulent stress parameterized with a mixing-length hypothesis and it is explained as follows:

$$\tau_t = \rho_a (\kappa z)^2 \left(\frac{\partial U}{\partial z} \right)^2 \tag{15}$$

where ρ_a is the air density, the von Karman constant (κ) is equal to 0.4, and $U(z)$ is the wind speed at height z.

The wave-dependent stress, τ_w, is large at the initial stages of wave growth when young wind–sea prevails in the wave field. This occurs immediately after an increase of the wind speed or change of the wind direction. Janssen (1991) derived the wave-induced

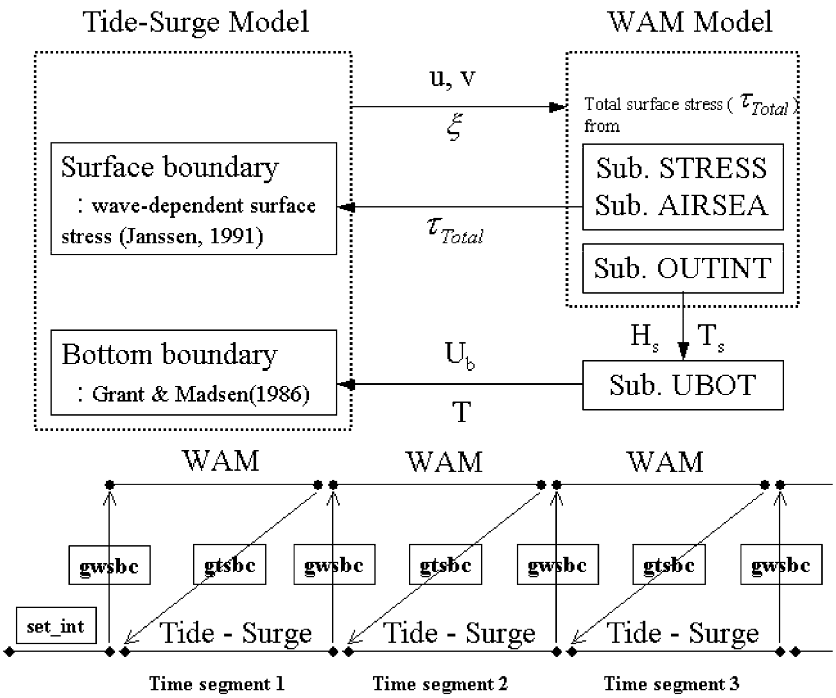

Fig. 4. Schematic diagram of synchronous coupling between WAM model and tide–surge model.

stress using the following wind profile in the presence of waves

$$U(z) = \frac{u*}{\kappa} \ln\left(\frac{z + z_e - z_0}{z_e}\right) \tag{16}$$

where $u*$ is the friction velocity, and z_0 and z_e are the roughness length in the absence of waves and the effective roughness length (a function of the wave-induced stress), respectively.

For the turbulent term of the stress, the mixing length hypothesis is assumed. If the wind profile (Eq. (16)) is differentiated, squared, and compared with the expression of the turbulent stress (Eq. (15)), at $z = z_0$, the relationship between z_0 and z_e is explained as

$$z_e = \frac{z_0}{\sqrt{1 - \tau_w(z_0)/\tau}} \tag{17}$$

where Eq. (14) and the friction velocity $(u* = \sqrt{\tau/\rho_a})$ are used.

Since drag coefficient (C_D) depends on the roughness length, τ is given by

$$\tau = C_D U^2(L) \tag{18}$$

where

$$C_D = \left(\frac{k}{\log(L/z_0)}\right)^2 \tag{19}$$

where k is the wave number, L is the mean height above the wave and the wave-induced stress, τ_w, is given by

$$\tau_w = \rho_w \int_0^{\infty} \int_0^{2\pi} \sigma S_{in}(f_r, \theta) \mathrm{d}f \, \mathrm{d}\theta \tag{20}$$

where σ is the angular frequency, f_r is the frequency, θ is the direction, ρ_w is the density of water, and S_{in} is the wind input source function.

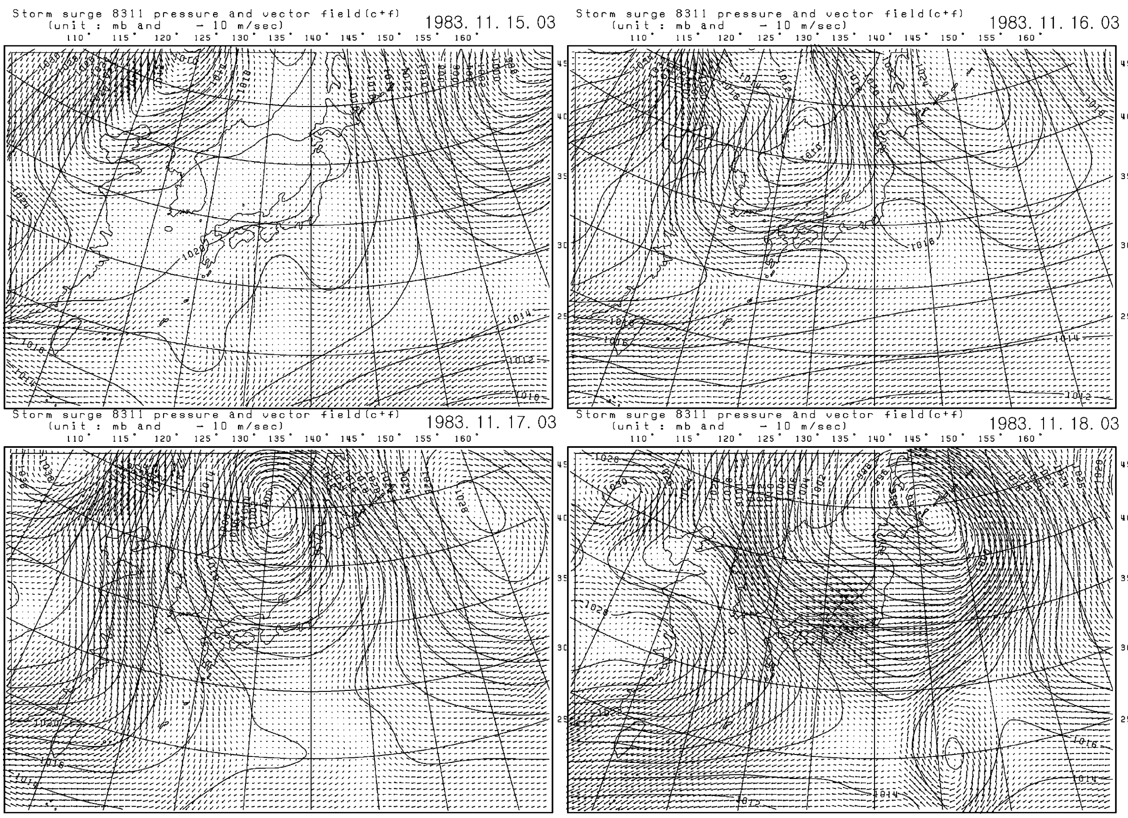

Fig. 5. Distribution of wind and pressure fields during winter monsoon in November 1983.

The wave-dependent stress τ_w is computed from S_{in}, which is based on an analytical approximation of the results obtained from quasi-linear theory of wave generation. Given the wind speed, $U(L)$, at L and τ_w and the surface roughness are determined from an iterative solution of Eqs. (17)–(20). The ratio, τ/τ_w, depends on the wave age and denotes the strength of the coupling between winds and waves. For extreme, young wind–sea, the surface roughness can be enhanced by as much as a factor of 10.

Given the $U(L)$ wind speed, τ_w, and the surface roughness are determined from iterative solution using set of equations with the algorithm provided within WAM model. There are general discrepancies between the present approach and conventional method (e.g. Smith and Banke, 1975) as illustrated in Fig. 3.

For the wave and bottom roughness conditions, it was determined that the effect of the steady current on the oscillatory stress component could be neglected, since it only influences τ_w, is in itself negligible to τ_c. The steady stress component (τ_c), on the other hand, is a strong function representing both waves and currents and therefore, the effective drag coefficient can be determined from an iterative process followed by the method of Grant and Madsen (1986).

The procedure is as follows.

(1) Assume C_R^n (stress enhancement factor) = 1.0. Determine $\tau = f\rho|\bar{u}|\bar{u}$, where the friction factor, f, is 0.0025, the air density, ρ, is 1025 kg/m^3, $\bar{u}$ is depth–mean velocity. Current shear velocity $(u_{*_c} = \sqrt{\tau/\rho})$ and current velocity $(u_c = \{\{u_{*_c}\}/\{\kappa\}\}\ln\{\{z\}/\{z_0\}\})$ with the bottom roughness ($z_0 = 0.1$ cm), reference level ($z = 100$ cm) were selected for the simplicity. This

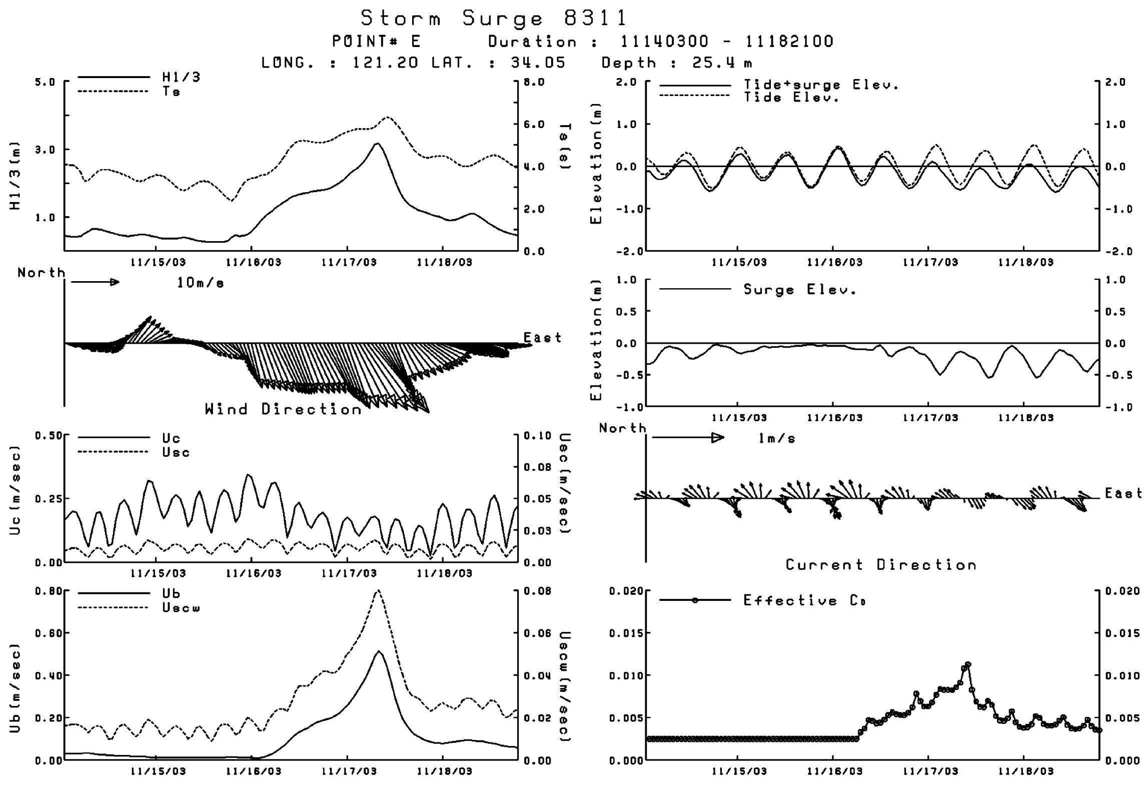

Fig. 6. Variation of wave, tide, and surge information at point E (depth = 15.1 m) during winter monsoon.

covers biological as well as most wave-formed ripple cases.

(2) Find a value of f_w (combined wave–current friction factor) corresponding to C_R^n by solving Eq. (21):

$$\frac{1}{4\sqrt{f_w}} + \log\frac{1}{4\sqrt{f_w}} = \log\left(\frac{C_R^n u_b}{\omega z_0}\right) - 1.65 + 0.24\left(4\sqrt{f_w}\right) \quad (21)$$

where radian frequency ($\omega = 2\pi/T_S$), where T_S is the wave period and u_b is wave induced orbital velocity.

(3) Calculate $u*_{wm}$ (enhanced wave shear velocity) from the following equation:

$$u*_{wm} = \sqrt{\tau_{wm}/\rho} = \sqrt{C_R^n}\sqrt{f_w/2}\cdot u_b \quad (22)$$

(4) Calculate $u*_c$ (current shear velocity) from the following equation:

$$u_c = \frac{u*_c}{\kappa}\left(\frac{u*_c}{u*_{cw}}\ln\frac{\delta_{cw}}{z_0} + \ln\frac{z}{\delta_{cw}}\right) \quad (23)$$

where $u*_{cw} = u*_{wm}\sqrt{C_R^n}$, $\delta_{cw} = 2l = 2(\kappa u*_{cw}/\omega)$, l is the scale of the wave boundary layer thickness.

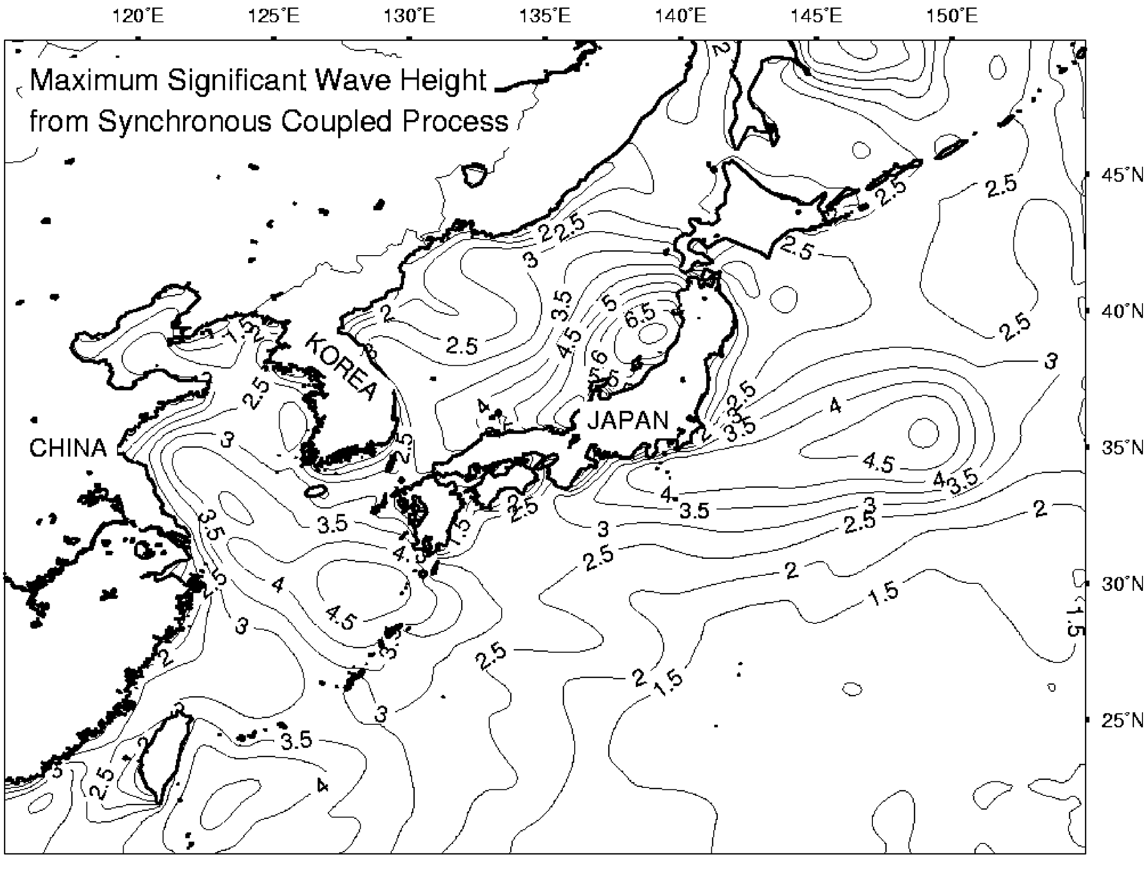

Fig. 7. Distribution of maximum significant wave height (m) during winter monsoon in November 1983.

(5) Calculate new C_R^{n+1} from the following equation:

$$u*_{\mathrm{cw}} = u*_{\mathrm{wm}}\left[1 + 2(u*_{\mathrm{c}}/u*_{\mathrm{wm}})^2\cos\phi + (u*_{\mathrm{c}}/u*_{\mathrm{wm}})^4\right]^{1/4} = \sqrt{C_R^{n+1}}u*_{\mathrm{wm}} \quad (24)$$

where ϕ denotes the angle between waves and current and is taken as collinear.

(6) If $(C_R^{n+1} - C_R^n)/C_R^{n+1} > 0.01$, go to step (2). Otherwise, calculate the effective drag coefficient, C_D.

2.4. Simulation procedures

For the tide and surge simulation, the vertically integrated equations for the tides and storm surges in spherical coordinates were used (Choi, 1986), while the WAM model (WAMDI Group, 1988) was used for wave computations. The synchronous-coupling scheme of the two models to explore the mutual interactions of wave–tide–surge processes is shown in Fig. 4. Resolution of the two models is identical as 1/12° in longitude and latitude covering inner NW Pacific including the East China Sea continental shelf and the East (Japan) Sea.

The following four steps are performed for synchronous simulation.

(1) The SET_INT subprogram of the coupled model generates the initial input data of the wave model including surface wind forcing. Before the wave model is coupled with the tide–surge model, the tide–surge model runs to confirm that tide with the duration of 3 days propagates to the entire modelled region.

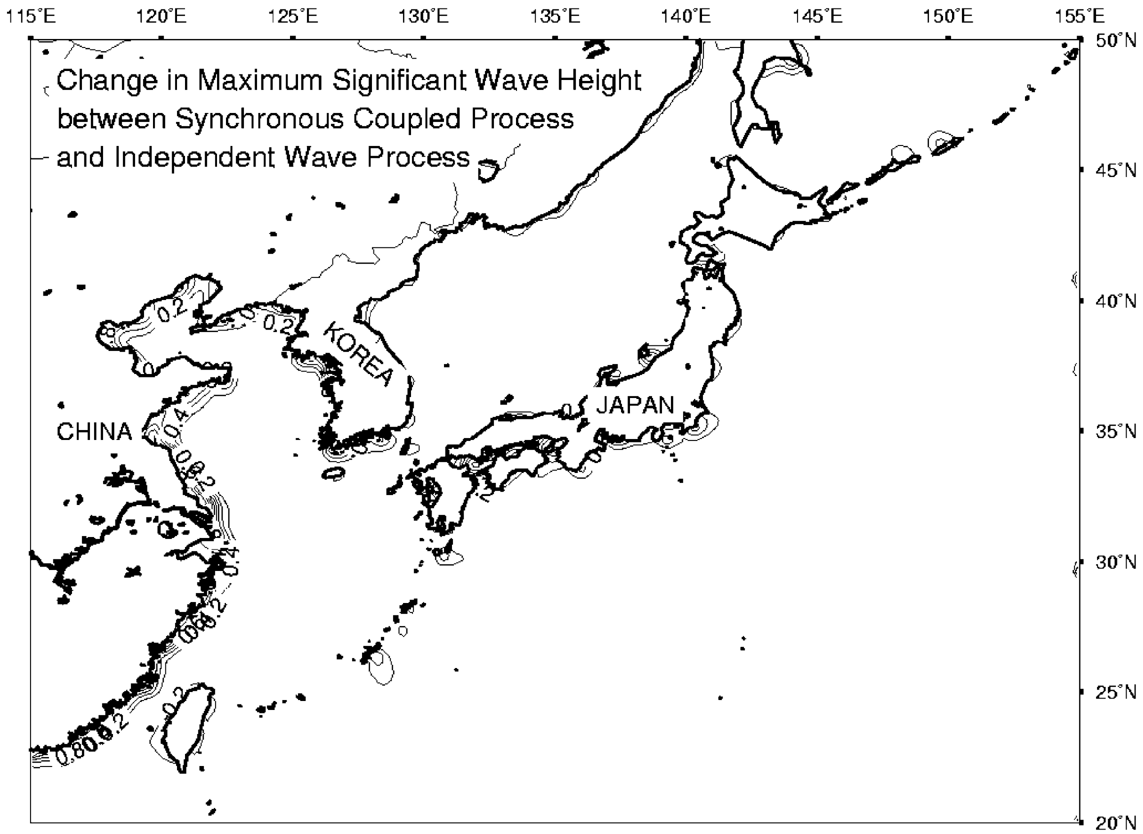

Fig. 8. Distribution of changes of significant wave height (m) between synchronously coupled model run and independent wave model run during winter monsoon.

(2) GWSBC subprogram is executed to obtain the mean value of the water surface elevation at the center and currents at the edge center of the each grid from the tide–surge model. Then, these mean values obtained from the tide–surge model are used for the input data of the wave model. Similarly, the GTSBC subprogram is executed to obtain the mean value of the wave information (wave height, period, and total surface stress) at four corners of the grid from the wave model. Similarly, these mean values are used for the input data of the tide–surge model.
(3) The wave model and the tide–surge model is performed with the constant time step. Time step of the tide–surge and wave model is 10 and 120 s, respectively. To exchange the information of these two models, time step of 120 s can be used. However, time step of 3600 s is selected for this study after making a series of numerical tests.
(4) In the coupled run, surface forcings for tide and surge model are prescribed by total surface stress considering wave-dependent drag, which is computed by WAM and atmospheric pressure gradient.

Steps (2)–(4) are repeated to obtain the wave information and currents at each time step.

3. Meteorological forcing input

For the present simulation, Grid Point Values (GPVs) of sea level pressure and air and sea surface temperature with 50-km intervals over the Northeast

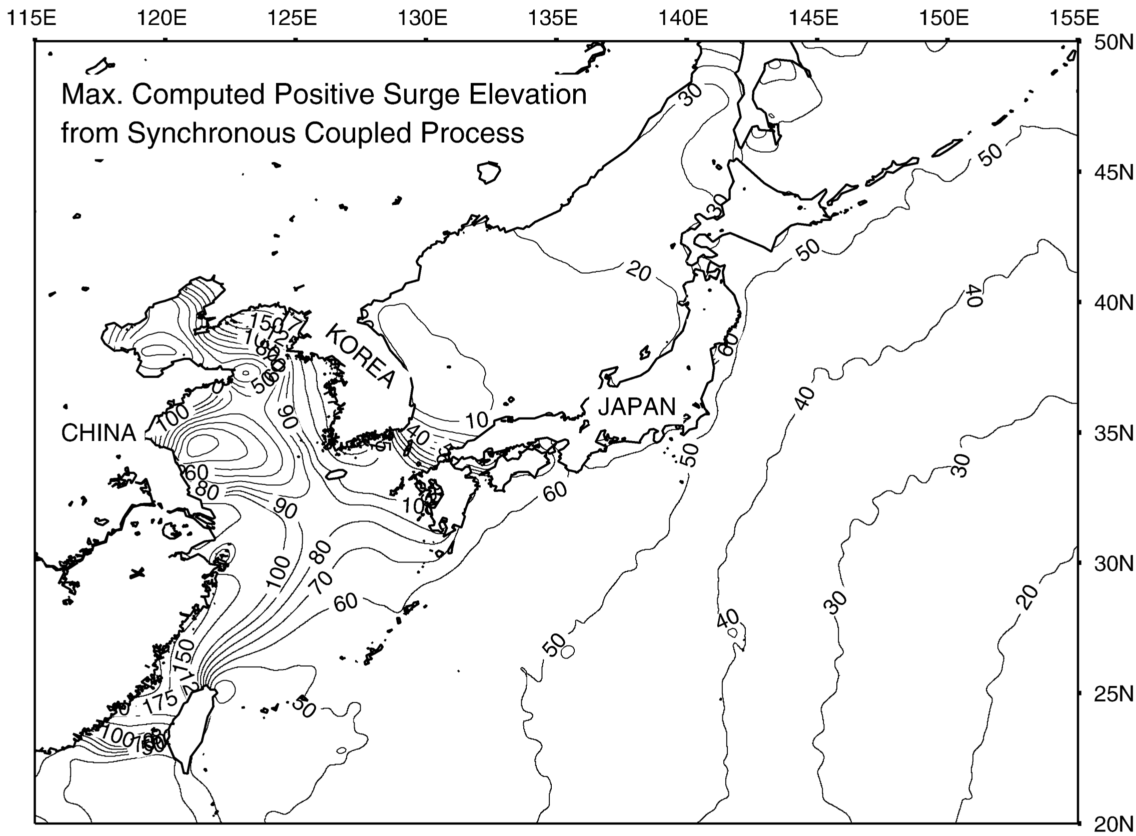

Fig. 9. Distribution of maximum positive surge height (cm) during winter monsoon in November 1983.

Asian seas were digitized by Japan Weather Association (JWA). Those values were interpolated to dense 1/12° grid resolution at 1-h intervals from six hourly dataset for the coupled model. The overall marine wind fields are computed by adopting Planetary Marine Boundary Layer model (Cardone, 1969). Temporal interpolation along the typhoon track was also performed. Fig. 5 shows the computed results of pressure and wind vector fields for the period of November 14–18 in 1983. A low-pressure center, forming over Mongolia on November 15, 1983, moved rapidly along a southeast track toward the East Sea. By November 16, the storm center was positioned in the middle of the East Sea and winds over the Yellow and the East China Seas speed over 10 m/s. The intensification of the storm center over Siberia and the high pressure cell over inner Mongolia generated a strong flow convergence over the Yellow Sea on November 17, where maximum wind speeds reached 20 m/s. By November 18, a newly formed high-pressure center over Shanghai dominated the Yellow Sea region with weaker westerly winds and northerly to northeasterly winds over the East China Sea. There are general agreements at selected stations C, D, and E with those computed by Graber et al. (1989). They employed the theoretical model (Hesselberg, 1915; Hesselberg and Sverdrup, 1915), relating with exchange coefficient determined by Bijvoet (1957) to compute marine surface wind for the same period and applied the finite-depth wind wave model of the Yellow Sea. Some discrepancies in wind fields resulting from this method and Cardone's PMBL model adopted in our study reflected in the model simulations.

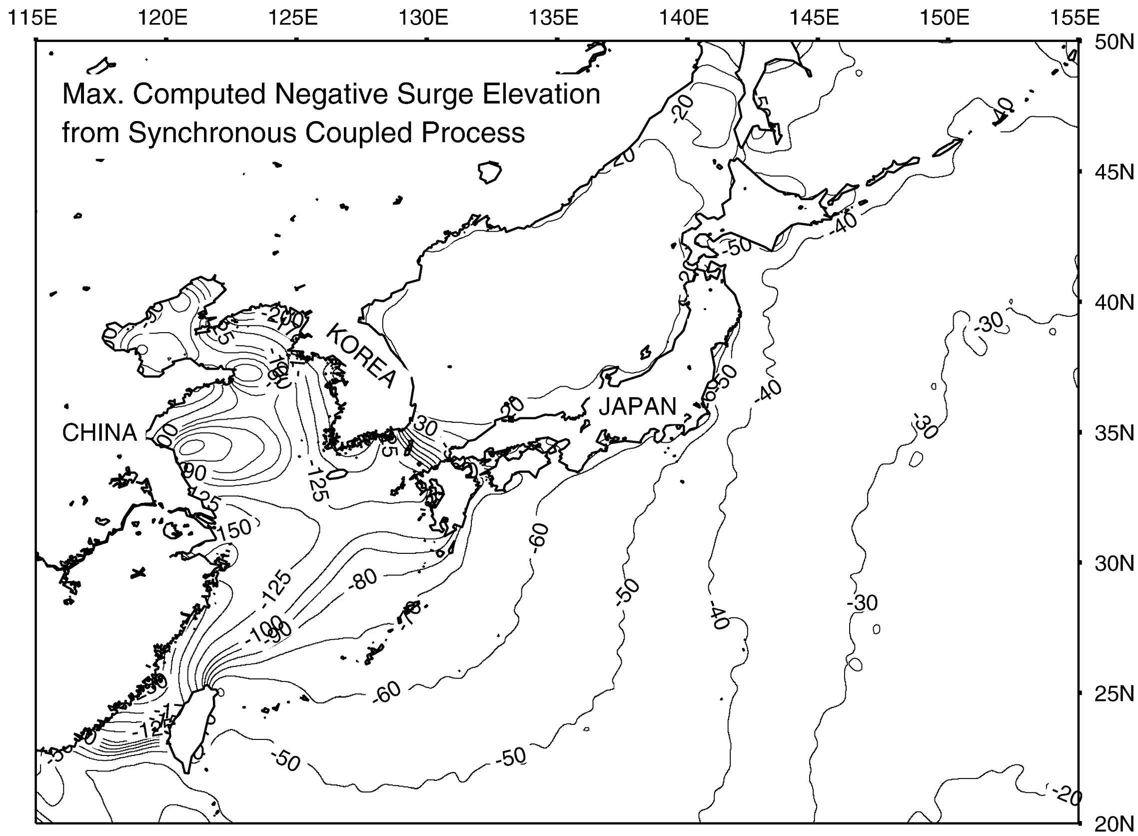

Fig. 10. Distribution of maximum negative surge height (cm) during winter monsoon in November 1983.

4. Model results

To investigate coupling effects of tides, storm surges, and wind waves, the simulation has been performed with an additional numerical experiment along with synchronous-coupling runs. The tide and surge model run the motion generated by the M_2, S_2, N_2, K_2, K_1, O_1, P_1, and Q_1 tidal constituents and an approximate surge based on the hydrostatic law, introduced on the open boundaries of the model together with forcing by surface wind stress and gradients of atmospheric pressure applied over the interior of the sea, was computed. This yielded the total motion due to tide and surge.

Fig. 6 shows the time series of the significant wave height (H_S), mean period (T_S), sea surface elevation (tide + surge and tide only), wind direction, surge elevation, depth–mean current ($\overline{u}$), current shear velocity (u_{*_c}), current direction, near-bottom wave orbital velocity (u_b), combined wave–current velocity ($u_{*_{cw}}$), and effective bottom drag coefficient (C_D) resulted from the synchronously coupled modelling showing variations at a point E of southern Shandong Peninsula during winter monsoon in November 1983. Fig. 6 shows the maximum wind speed exceeds 15 m/s at point E (121.20°E, 34.05°N). And the significant wave height does exceed 3 m and the mean wave period remains roughly range of 5–6 s. However, the near-bottom orbital velocity and the combined wave–current velocity reach as high as 0.4 and 0.08 m/s, respectively. These large flows are also reflected in the bottom friction exceeding 0.01. The combined wave–current-induced bottom velocity and effective

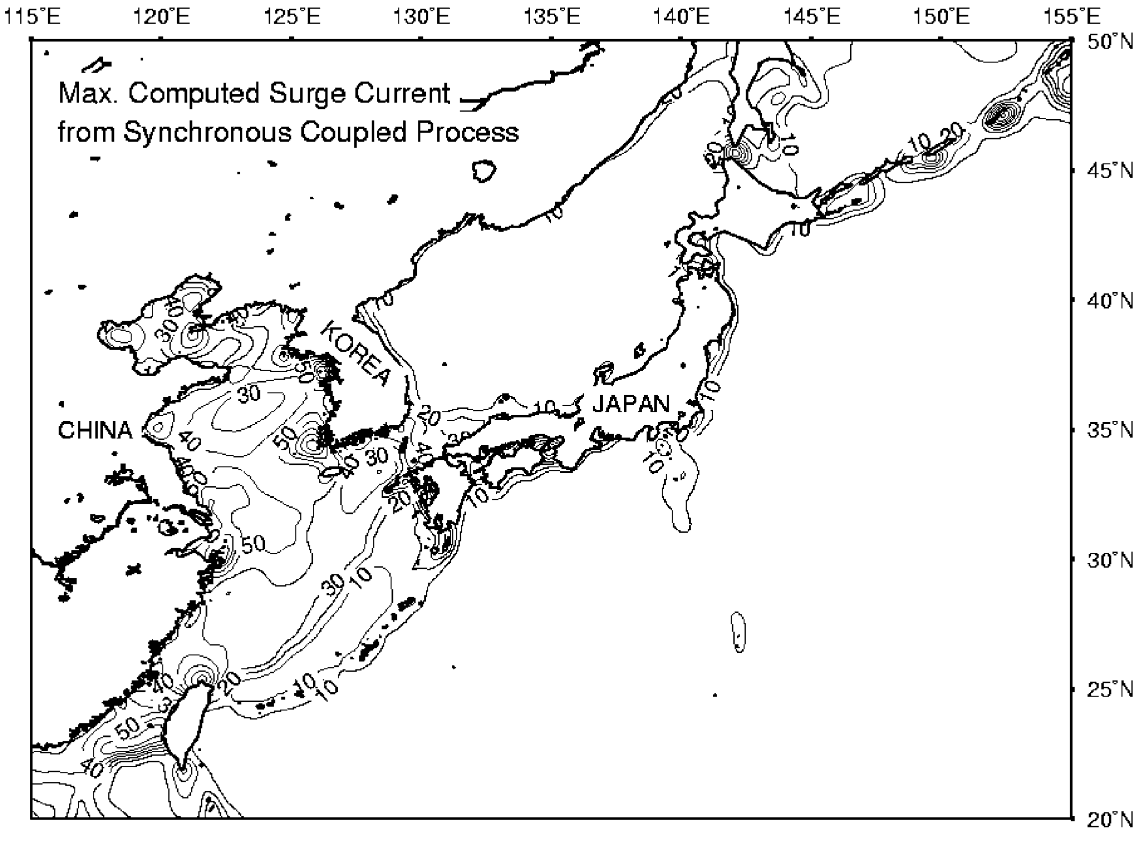

Fig. 11. Distribution of maximum surge current (cm/s) during winter monsoon in November 1983.

bottom drag coefficient were increased in the shallow waters during the strong storm conditions. The significant wave height exceeds 2.5 m and the mean wave period remains at relatively constant value of 6–7 s for the nearly 1-day period of high winds at point C (123.65°E, 34.77°N), shown in Fig. 1. The winds hold from the northwest for almost a day while intensifying to speed in excess of 15 m/s. The combined wave–current velocity is about 0.05 m/s at the bottom constant. The maximum negative surge elevation has about − 0.5 m. At point D (122.27°E, 34.45°N), in a similar pattern with point C, the wave heights grow up to 3 m with wave periods of 7 s and negative surge elevation is almost − 0.5 m. However, at this point, the near-bottom orbital velocity and the combined wave–current velocity are about 0.1 m/s and 0.02 m/s, respectively, and the effective drag coefficient reaches up to about 0.005 or more.

The distribution of the maximum significant wave height during winter monsoon from synchronously coupled simulation is shown in Fig. 7. This figure shows, the maximum significant wave height occurs around the southwestern part of the Kyushu with the wave height of 4.5 m and at the eastern coast of the Honshu with the wave height of 6.5 m or more. Fig. 8 shows the change between synchronously coupled model run and independent (non-coupled) wave model run for significant wave height. The change of significant wave height is substantially increased to the significant wave height of 1.0–1.5 m and 0.5 m at the southern coasts of

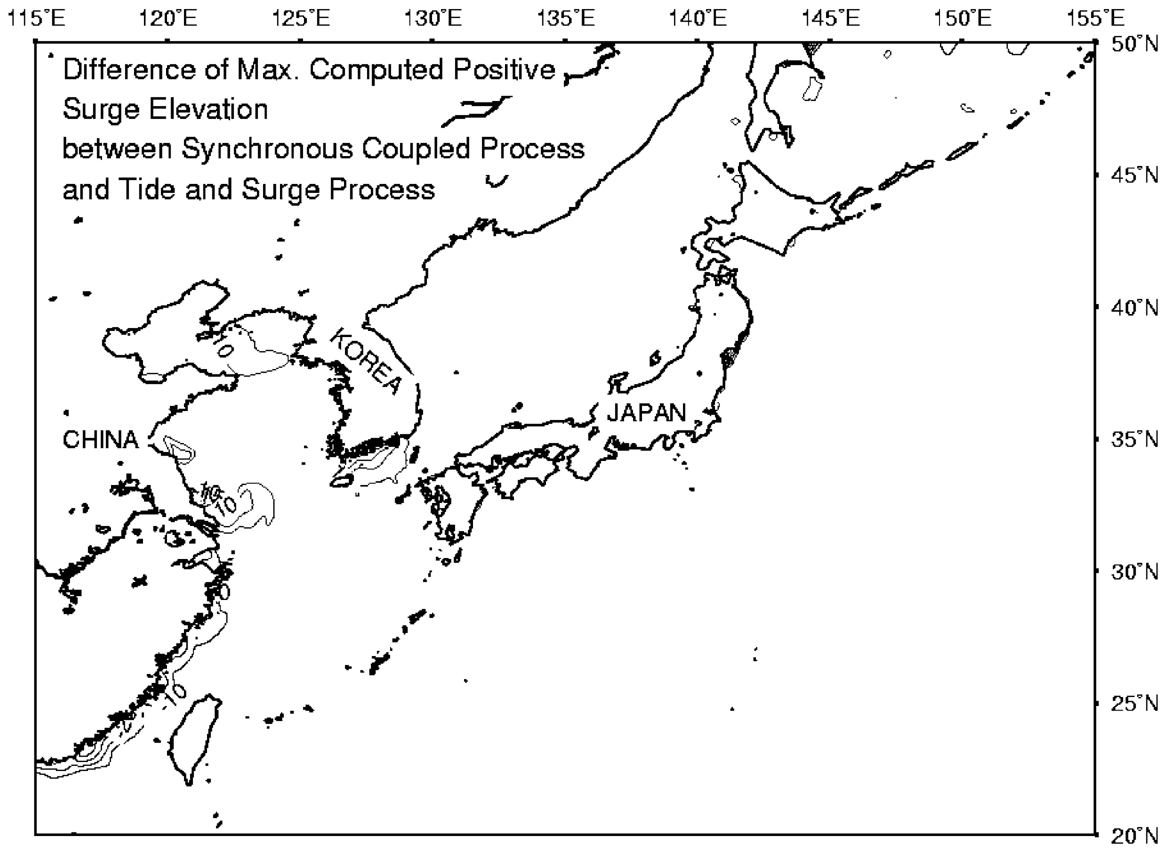

Fig. 12. Distribution of difference of maximum positive surge height (cm) between synchronously coupled model run and tide–surge model run during winter monsoon in November 1983.

Shandong in China and the western coasts in Korea, respectively.

The distribution of the computed maximum positive and negative surge elevation and current during winter monsoon from synchronously coupled simulation is shown in Figs. 9–11. As shown in Fig. 9, the elevation of water surface increases up to 1.0 m around the southern coasts of Shandong in China, while the elevations of the Hangzhou Bay in Chinese coast and the western coasts in Korea reach up to 1.0 and 1.25–1.50 m, respectively. The computed maximum negative surge elevations are in the range from − 1.5 to − 2.0 m for the western and southern coasts in Korea, − 1.25 to − 1.50 m for the Hangzhou Bay, and − 1.5 to − 2.0 m for the Fujian coasts in China (Fig. 10). Fig. 11 shows, the computed maximum surge currents occur around the southwestern part of Korea with 0.5 m/s and the Changjiang river of China with 0.6 m/s. The change between synchronously coupled model run and tide–surge model run for positive surge elevation is shown in Fig. 12. In this figure, the elevation of water surface for the entire modelled region is not changed except for about 0.1 m around the Changjiang river in China and 0.1–0.2 m at the southern coasts in Korea, respectively, and the level has substantially great amount of elevation changes of − 0.1 m around the Fujian coasts in China. Fig. 13 shows the change between synchronously coupled model run and tide–surge model run for maximum negative surge elevation. The elevation decreased to about 0.1 m around the northern part of Yellow Sea. The elevation of maximum surge current

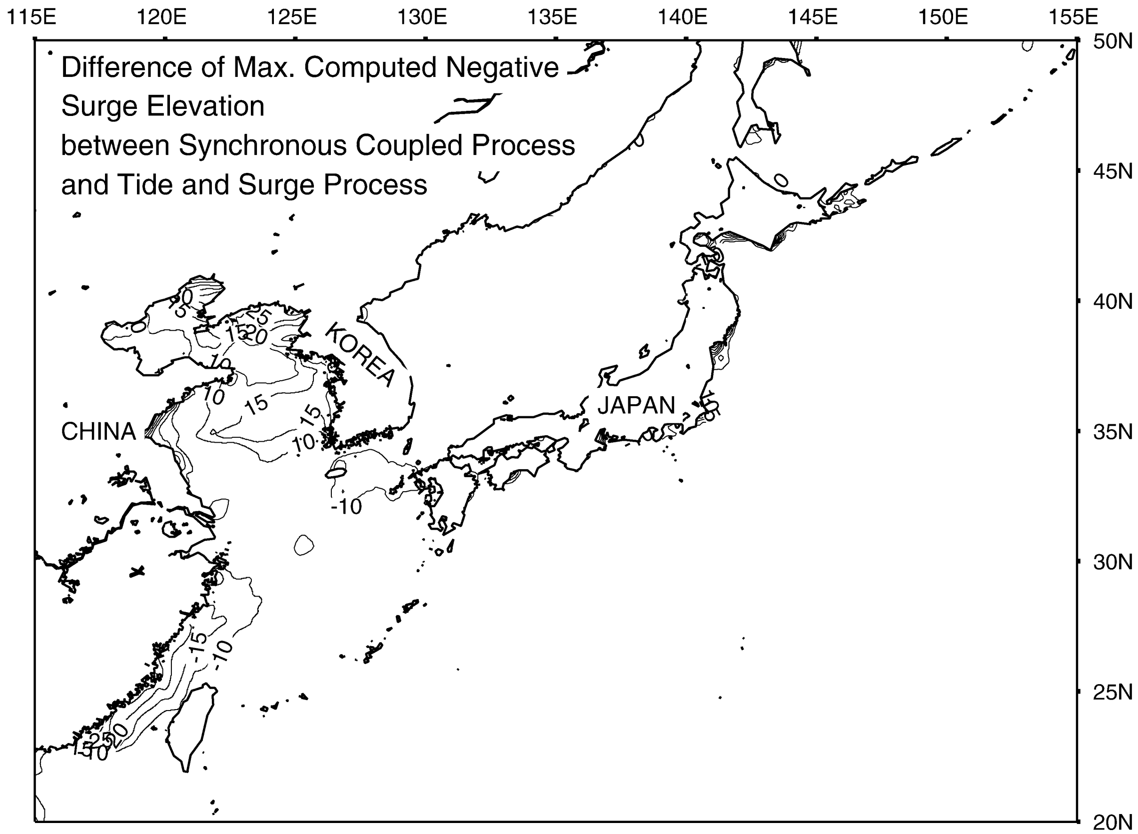

Fig. 13. Distribution of difference of maximum negative surge height (cm) between synchronously coupled model run and tide–surge model run during winter monsoon in November 1983.

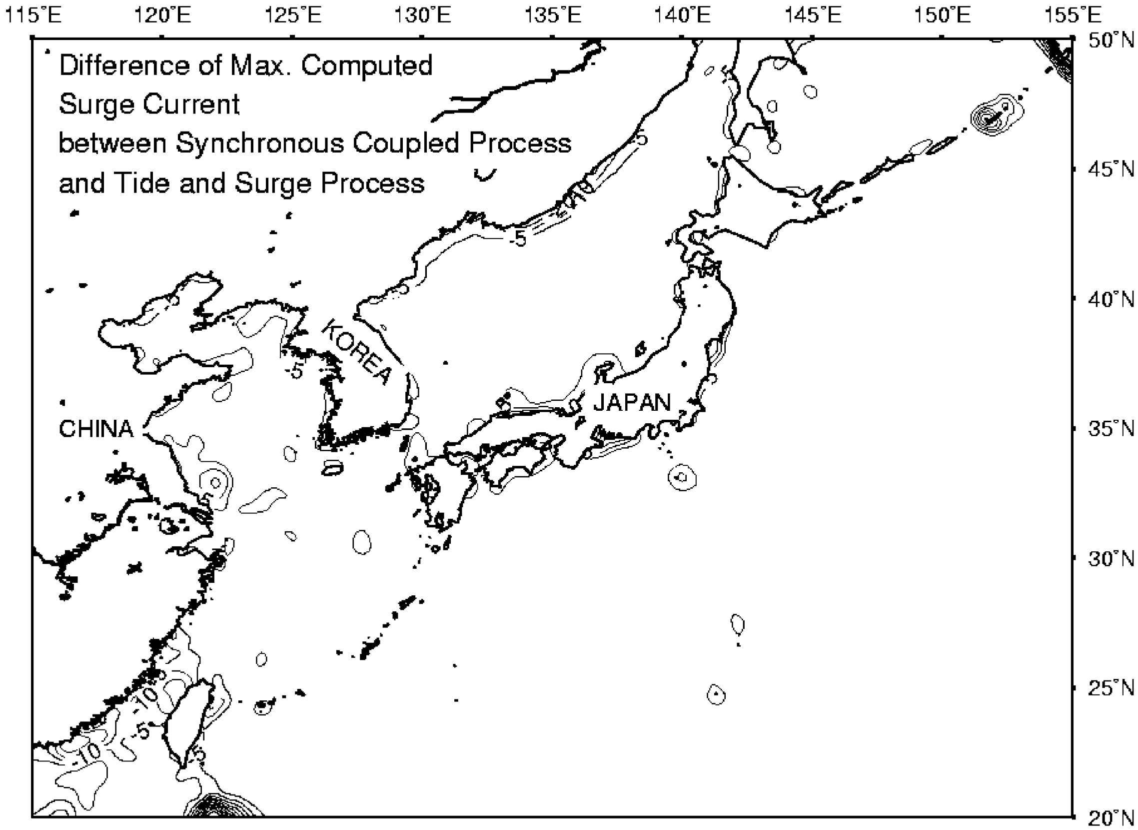

Fig. 14. Distribution of difference of maximum surge current (cm/s) between synchronously coupled model run and tide–surge model run during winter monsoon in November 1983.

results in a decrement of the current, −0.1 m/s, around the western part of Taiwan as shown in Fig. 14.

5. Conclusion

A synchronously coupled wave–tide–surge model developed in this study by considering the effect of surface waves covers the tide and surge simulation through an effective bottom drag coefficient calculated by using the theory of Grant and Madsen (1986) and while the unsteadiness of surface elevation and currents due to tide and surge are used for the wave computation. In this study, the storm surge in November 1983 was reasonably well simulated based on the established model as a first attempt. At this stage, the comparisons in this paper are intended for, between coupled and noncoupled runs of the model for emphasizing sensitivity showing that there are clear differences and feasibility of accommodating the BBL model adopted. Further improvement is being progressed to incorporate the stratified bottom conditions (Glenn and Grant, 1987; Styles and Glenn, 2000) to limit the local increase of effective bottom friction factor and replace the two-dimensional to three-dimensional tide and surge model with the verification by comparing the results from the model with the more detailed field measurement project, which has been formulated in this region yet.

Acknowledgements

The research was performed as a part of the second phase (1998–2000) of Natural Hazard Prevention Research, funded by the Science and Technology through KISTEP (Korea Institute of Science and Technology Evaluation and Planning) and Group for Natural Hazard Prevention Research.

References

Bijvoet, H.C., 1957. A new overlay for the determination of the surface wind over sea from surface weather charts. Kononklijk Nederlands Meteorologicsh Instituut, Mededelingen en Verhandelingen 7, 38 pp.

Cardone, V.J., 1969. Specification of the wind distribution in the marine boundary layer for wave forecasting. Report GSL-TR 69-1, New York University School of Engineering and Science.

Charnock, H., 1955. Wind stress on a water surface. Q. J. R. Meteorol. Soc. 81, 639–640.

Choi, B.H., 1980. A tidal model of the Yellow Sea and the Eastern China Sea. Korea Ocean Research and Development Institute, Tech. Report 80-02, 72 pp.

Choi, B.H., 1986. Surge hindcast in the East China Sea. Prog. Oceanogr. 17, 67–81.

Choi, B.H., 1987. Development of tide and surge models of the Yellow Sea for coastal engineering application. Proceedings of the Second Conference on Coastal and Port Engineering in Developing Countries, China Ocean Press, Beijing, China, pp. 1880–1894.

Choi, B.H., 1993. Development of tidal models at Sungkyunkwan University. Proceedings of the Workshop on Tidal and Oil Spill Modeling. Pohang Institute of Science and Technology, Korea, pp. 81–101.

Choi, B.H., Ko, J.S., 1994. Modeling of tides in the East Asian Marginal Seas. J. Korean Soc. Coast. Ocean Eng. 6 (1), 94–108.

Choi, B.H., Kim, K.O., Eum, H.M., 2002. Digital bathymetric and topographic data for neighboring seas of Korea. J. Korean Soc. Coast. Ocean Eng. 14, 41–50.

Davies, A.M., Lawrence, J., 1994. Examining the influence of wind and wave turbulence on tidal currents, using a three-dimensional hydrodynamic model including wave–current interaction. J. Phys. Oceanogr. 24, 2441–2460.

Doodson, A.T., 1921. The harmonic development of the tide-generating potential. Proc. R. Soc. A 100, 305–329.

Glenn, S.M., Grant, W.D., 1987. A suspended sediment stratification correction for combined wave and current flows. J. Geophys. Res. 92 (C8), 8244–8264.

Graber, H.C., Madsen, O.S., 1985. A parametric wind wave model for arbitrary water depths. In: Toba, Y., Mitsuyasu, H. (Eds.), The Ocean Surface: Wave Breaking, Turbulent Mixing and Radio Probing. Reidel, Dordrecht, Netherlands, pp. 193–199.

Graber, H.C., Beardsley, R.C., Grant, W.D., 1989. Storm-generated surface waves and sediment resuspension in the East China and Yellow Seas. J. Phys. Oceanogr. 19, 1039–1059.

Grant, W.D., Madsen, O.S., 1986. The continental shelf bottom boundary layer. Annu. Rev. Fluid Mech. 18, 265–305.

Günther, H., Hasselmann, S., Janssen, P.A.E.M., 1992. The WAM model Cycle 4, Report No. 4, Hamburg.

Heaps, N.S., 1983. Storm surges 1967–1982. Geophys. J. R. Astron. Soc. 74, 331–376.

Hesselberg, T., 1915. Über die Beziejung Zwischen Luftdruck und Wind im niehtstationären Fall. Veroffentl. D. Geophys. Inst. Univ. Leipz., Ser. 2 7, 175–201.

Hesselberg, T., Sverdrup, H.V., 1915. Die Reibung in der Atmosphäre. Veröffentl. D. Geophys. Inst. Univ. Leipz., Ser. 2 10, 241–309.

Janssen, P.A.E.M., 1991. Quasi-linear theory of wind wave generation applied to wave forecasting. J. Phys. Oceanogr. 21, 1631–1642.

Komen, G.J., Cavaleri, L., Donelan, M., Hasselmann, K., Hasselmann, S., Janssen, P.A.E.M., 1994. Dynamics and Modelling of Ocean Waves. Cambridge Univ. Press, Cambridge.

Li, Y.S., Zhang, M.Y., 1997. Dynamic coupling of wave and surge models by Eulerian–Lagrangian method. J. Waterw. Port Coast. Ocean Eng. 123 (1), 1–7.

Mastenbroek, C., Burgers, G., Janssen, P.A.E.M., 1993. The dynamical coupling of a wave model and a storm surge model through the atmospheric boundary layer. J. Phys. Oceanogr. 23, 1856–1866.

Monbaliu, J., Hargreaves, J.C., Carretero, J.C., Gerritsen, H., Flather, R., 1999. Wave modeling in the PROMISE project. Coast. Eng. 37, 379–407.

Monbaliu, J., Padilla-Hernández, R., Hargreaves, J.C., Albiach, J.C.C., Luo, W., Sclavo, W., Günther, H., 2000. The spectral wave model, WAM, adapted for applications with high spatial resolution. Coast. Eng. 41, 41–62.

Moon, I.J., 2000. Development of a coupled ocean wave-circulation model and its applications to numerical experiments for wind waves, storm surges and ocean circulation of the Yellow and East China Seas. PhD thesis, Seoul National Univ., Korea.

Ozer, J., Padilla-Hernández, R., Monbalin, J., Alvarez Fanjul, E., Carretero Albiach, J.C., Osuna, P., Yu Jason, C.S., Wolf, J., 2000. A coupling module for tides, surges and waves. Coast. Eng. 41, 95–124.

Prandle, D., 2000. Operational oceanography in coastal waters. Coast. Eng. 41, 1–3.

Robert, K.V., Weiss, N.O., 1967. Convective difference schemes. Math. Comput. 20, 272–299.

Smith, S.D., Banke, E.G., 1975. Variation of the sea surface drag coefficient with wind speed. Q. J. R. Meteorol. Soc. 101, 665–673.

Styles, R., Glenn, S.M., 2000. Modeling stratified wave and current bottom boundary layers on the continental shelf. J. Geophys. Res. 105 (C10), 24119–24139.

Tolman, H.L., 2002. Alleviating the garden sprinkler effect in the wind wave models. Ocean Model. 4, 269–289.

WAMDI group, 1988. The WAM model—a third generation ocean wave prediction model. J. Phys. Oceanogr. 18, 1775–1810.

Zhang, M.Y., Li, Y.S., 1996. The synchronous coupling of a third-generation wave model and a two-dimensional storm surge model. Ocean Eng. 23 (6), 533–543.